JOURNAL OF GEOPHYSICAL RESEARCH, VOL. 112, D04104, doi:10.1029/2006JD007213, 2007

Investigation of a "wall" wave event

Feng Li,[1,2] Gary R. Swenson,[3] Alan Z. Liu,[3] Michael Taylor,[4] and Yucheng Zhao[4]

Received 17 February 2006; revised 28 July 2006; accepted 31 August 2006; published 20 February 2007.

[1] A bright airglow event was observed at Maui, Hawaii, on the night of 11–12 August 2004 with multiple instruments including a Na wind/temperature lidar, an airglow imager, and a mesospheric temperature mapper. The characteristics of this event were investigated with measurements from these instruments. Analysis showed that this event was caused by a large-amplitude, upward-propagating gravity wave with a period of about 4–5 hours and a vertical wavelength of about 20 km, i.e., a "wall" wave. This wall wave induced dramatic changes in temperature (60 K), airglow intensity (doubled in the OH and tripled in the O_2 emissions), and Na abundance (tripled). It experienced strong dissipation and induced large downward heat flux with values about an order of magnitude larger than the annual mean. The wave also carried large momentum flux ($\sim$70 m^2 s^{-2}).

Citation: Li, F., G. R. Swenson, A. Z. Liu, M. Taylor, and Y. Zhao (2007), Investigation of a ''wall'' wave event, *J. Geophys. Res.*, *112*, D04104, doi:10.1029/2006JD007213.

1. Introduction

[2] Wave-like disturbances have been routinely measured in mesopause airglow emissions. The most commonly observed disturbances are quasi-monochromatic wave bands and ripples. Both wave bands and ripples have been extensively studied and their origins are now well understood. Bands often appear as a train of wave fronts with horizontal wavelength on the order of tens of kilometers, while ripples are very fine-scale structures with horizontal separations, usually <15 km. It is now known that bands are caused by gravity waves originated from the lower atmosphere, and ripples are generated in situ by convective or dynamical instabilities [e.g., *Taylor and Hapgood*, 1990; *Swenson and Mende*, 1994; *Taylor et al.*, 1997; *Walterscheid et al.*, 1999; *Hecht*, 2004; *Li et al.*, 2005].

[3] In addition to bands and ripples, there exist unusual spectacular events in airglow emissions [e.g., *Taylor et al.*, 1995; *Swenson and Espy*, 1995; *Swenson et al.*, 1998; *Smith et al.*, 2003]. These events are characterized by a leading front with enhanced amplitude, which is followed by quasi-monochromatic wave trains. Dramatic changes in airglow intensity and temperature are often accompanied with the passage of the leading front. These events are sometimes referred to as bright wave events or mesospheric "fronts" [*Brown et al.*, 2004]. The events are marked with a high contrast in brightness with a very dim airglow followed by a very bright airglow. There are very different opinions, however, as to what physical process is responsible for these observations. *Dewan and Picard* [1998] suggested that the leading front was a mesospheric "bore", while *Swenson et al.* [1998] argued that it was the leading edge of a large-amplitude gravity wave. The so-called "wall" wave refers to a very pronounced airglow enhancement or a step increase in airglow brightness observed in airglow images. Despite the completely different nature, both theories can successfully explain most of the observed features.

[4] Since the two hypotheses were introduced, there are other reports of the mesospheric bores [*Smith et al.*, 2003, 2005; *Brown et al.*, 2004]. The "wall" wave interpretation has only been invoked to explain one observation in Brazil [*Medeiros et al.*, 2001] as well as an event observed in the region of Hawaii in 1993 [*Swenson and Espy*, 1995; *Swenson et al.*, 1998]. These studies often use measurements from multiple ground-based remote sensing instruments, but most lack high-resolution wind measurements. Detailed observations of wind, temperature and density with altitude and time are important to determine the geophysical process involved. It should be emphasized that wind observations provide crucial information of the vertical structures and intrinsic properties of the disturbances, and hence they are essential for accurately interpreting the nature of these high-contrast events.

[5] The Na wind/temperature lidar coupled with a large telescope is uniquely capable of making measurements with high temporal/spatial resolutions which are necessary to resolve these waves. On the night of 11–12 August 2004, a bright event was recorded by airglow observations at Maui, HI (20.7°N, 156.3°W). A Na wind/temperature lidar was also in operation on this night. The lidar temperature and wind profiles, along with simultaneous measurements from a colocated all-sky imager and a mesospheric temperature mapper provide a unique data set to investigate this event.

[6] In this paper, we show that this bright event was caused by a wave that had features similar to the wall wave described by *Swenson et al.* [1998]. The observations as a

[1]Department of Atmospheric Sciences, University of Illinois at Urbana-Champaign, Urbana, Illinois, USA.
[2]Now at Geophysical Fluid Dynamics Laboratory, Princeton, New Jersey, USA.
[3]Department of Electrical and Computer Engineering, University of Illinois at Urbana-Champaign, Urbana, Illinois, USA.
[4]Center for Atmospheric and Space Sciences, Utah State University, Logan, Utah, USA.

0148-0227/07/2006JD007213

whole indicate that it was an upward-propagating large-amplitude long-period gravity wave. The wave induced dramatic changes in temperature (60 K) and airglow intensity (doubled in OH and tripled in O_2 airglow intensity). The underlying mechanisms for these large changes are discussed.

2. Instrumentation and Data

2.1. Na Wind/Temperature Lidar

[7] The University of Illinois Na wind/temperature lidar has been operated in a seasonal campaign mode since January 2002 from the summit of Mt. Haleakala on Maui, HI. Details of the instrumentation can be found in *Chu et al.* [2005]. Coupled with a steerable 3.67 m diameter astronomical telescope at the Air Force Maui Optical Station, the lidar system measures the line-of-sight (LOS) Na density, Doppler temperature, and Doppler wind profiles in the 80–105 km height range. In a normal operating mode, the lidar is pointed to the zenith (Z), and 30° off the zenith toward north (N), east (E), south (S) and west (W) in ZNEZSW sequence. Horizontal winds are derived from off-zenith LOS wind profiles, while the zenith LOS wind gives the vertical wind. The temporal resolution of measurements is ~2 min. On the night of 11–12 August 2004, the Na lidar made ~10 hours of measurements (0540–1540 UT).

2.2. OH All-Sky Imager

[8] The University of Illinois all-sky airglow imager was colocated with the lidar system on Mt. Haleakala. This imager is similar to the airglow imaging system described by *Rezaul and Swenson* [1999]. It incorporates an all-sky lens with an Apogee 1024 × 1024 CCD camera to take images of the all sky field. A broadband filter (750.0–930.0 nm with a notch at 865.0 nm) is used to measure the mesospheric hydroxyl (OH) airglow emission which is centered at a mean altitude of ~89 km. The exposure time is 60 sec and images are taken every 2 min. The images are binned to 512 × 512 pixels to increase the signal to noise ratio. On this night, 270 images were taken from 0600 to 1500 UT.

2.3. Mesospheric Temperature Mapper

[9] The Utah State University Mesospheric Temperature Mapper (MTM) is a high-performance imaging system capable of precision measurements of the intensity and rotational temperature, of the near infrared OH and O_2 nightglow emission layers which occur at nominal peak altitudes of ~89 and ~94 km respectively. Briefly, the MTM utilizes a high quantum efficiency CCD array coupled to a wide-angle telecentric lens system (90° field of view centered on the zenith) to observe selected emission lines in the OH (6,2) Meinel band and the O_2 (0,1) Atmospheric band. Sequential measurements were made using a set of narrow band ($\Delta\lambda$ ~1.2 nm) filters centered on the OH P1(2) and P1(4) lines at 840 and 846.5 nm and two well-defined regions of the O_2 (0,1) Atmospheric band at 866 and 868 nm. Each emission was observed for 60 sec followed by a background sky measurement at 857 nm, resulting in a cycle time of ~5.5 min. The data were spatially summed on the CCD to form a 128 × 128 super pixel image with a resultant zenith pixel footprint of ~0.9 × 0.9 km at 90 km altitude. Rotational temperatures were computed separately for the OH and the O_2 emissions using the well-established "ratio method", as described by *Meriwether* [1984]. On the basis of typical OH and O_2 emission levels measured at Maui, the precisions of the measurements were determined to be <0.5% (in 1 min) for the individual line emission intensities, and <1–2 K (in 3 min) for the derived OH and O_2 rotational temperatures.

[10] Measurements of OH (6,2) and O_2 (0,1) Atmospheric band intensity and rotational temperature were obtain from ~0600 to 1500 UT on this night.

3. Results

3.1. All-Sky Imager Observations

[11] A bright wave was observed by the all-sky airglow imager on the night of 11–12 August 2004. The wave first appeared at the SW horizon at ~0700 UT and propagated toward the ENE. Historically, waves observed in the Northern Hemisphere summer have been noted to propagate from the northwest [e.g., *Taylor et al.*, 1995; *Swenson et al.*, 1998; *Smith et al.*, 2003], so the direction of this event is somewhat unusual. Its leading front passed the zenith at about 0900 UT. Figure 1 shows a sequence of flat-fielded, unwarped all-sky images between 0840 and 0940 UT. The leading front is most clearly seen in the first four images, which separates a dark region to its NE from a bright region to its SW. The bold arrow in the image of 0844 UT indicates the propagation direction of the bright wave. The leading front propagated toward the ENE (20° anticlockwise of east) at an observed phase speed of ~45 ms^{-1}. Several high-frequency wavefronts were behind and appeared to be phase locked with the leading front. The most striking feature in Figure 1 is the sharp increase of airglow brightness, not just at the leading front, but within the whole sky, during the passage of the bright wave.

[12] Figure 2 shows the same series of images, but each image was normalized such that the high-frequency waves stand out. Initially there were 3–4 wavelengths trailing the leading bright front, and lacked coherence before 0900 UT. The high-frequency wave train became more coherent and evolved to cover almost the entire 300 × 300 km area with 9–10 wavelengths by 0940 UT. The average horizontal wavelength of the high-frequency wave was ~20 km, and the relative amplitude was ~3%. The wave train was phase locked with the leading front with an observed phase speed of ~45 ms^{-1}. These parameters are typical for high-frequency quasi-monochromatic waves [*Swenson et al.*, 1999].

[13] It is clear, by comparing Figures 1 and 2, that the bright wave characterized by the leading front of enhanced airglow intensity, and the high-frequency wave train are two different wave structures. The sharp intensity increase of the entire sky shown in Figure 1 suggests that the former is a large-amplitude dynamical structure.

3.2. MTM Observations

[14] Dramatic changes of airglow intensity and rotational temperature were recorded by the MTM during the passage of the bright wave. Figure 3a shows the time histories of the zenith OH and O_2 band intensities through this night. The O_2 emission brightness underwent a jump between ~0730 and 0830 UT, during which the intensity increased 175%. The O_2 brightness remained high until ~0930 UT, and then

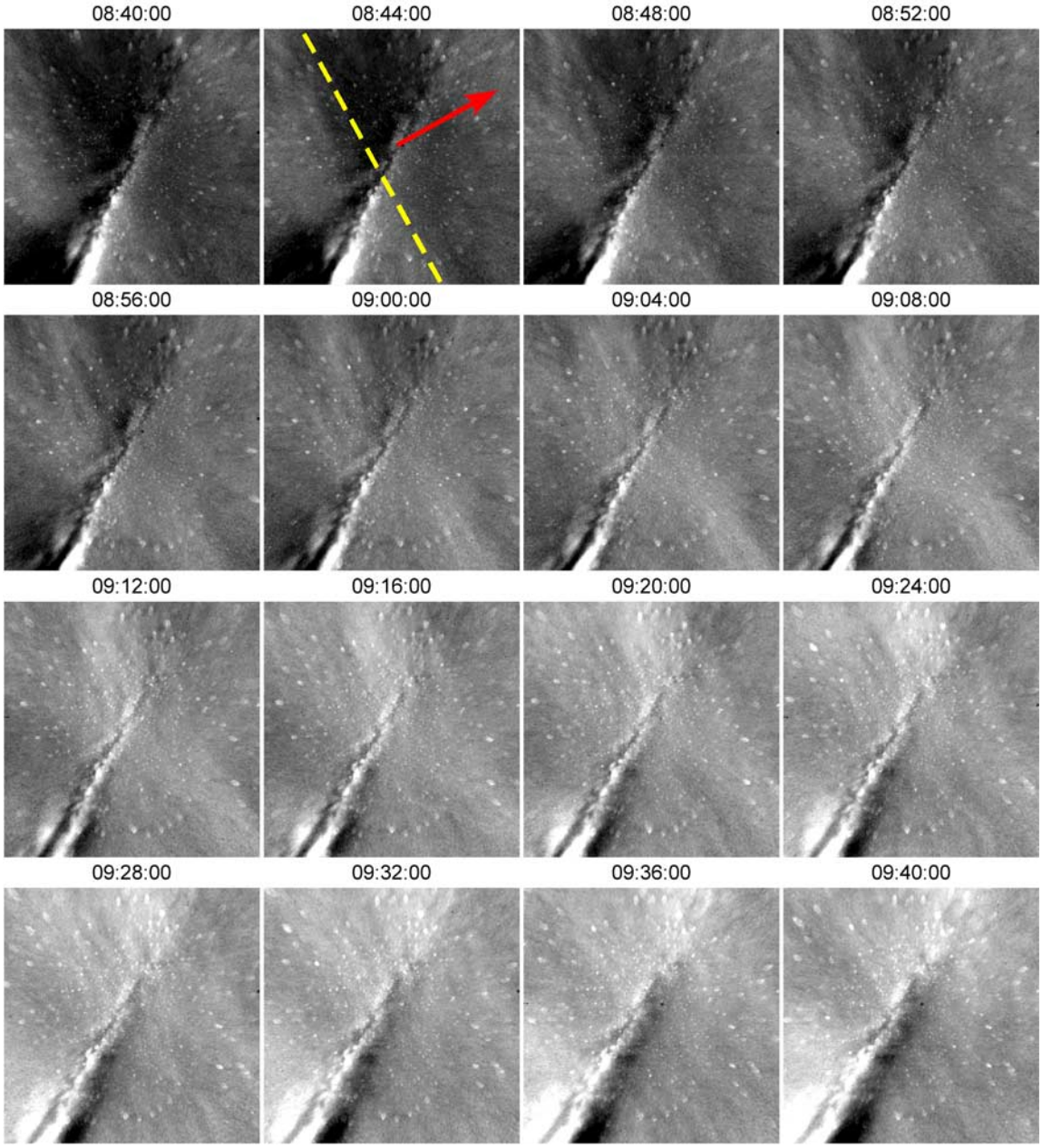

Figure 1. A sequence of flat-fielded all-sky OH images. Each image is projected to a geographic reference frame with a spatial dimension of 300 × 300 km. The background, which is the mean of the 16 images, was subtracted from each image. In the image at 0844 UT, the yellow dashed line indicates the position of the leading front of a bright wave which separates a dark region to its NE and a bright region to its SW. The red bold arrow indicates the propagation direction of the "wall" wave. The very bright band structure extending from the zenith to the southwest of the sky is the Milky Way.

began to decrease, reaching a local minimum at 1100 UT. The OH emission had very similar temporal variations, except that the brightness change lagged the change in the O_2 emission by about 1 hour. The sharp increase in the OH brightness started at ~0820 UT, and ended after ~0920 UT. During this period, the OH intensity underwent a 90% increase. Note that the maximum OH airglow brightness was reached at about the same time when the leading front of the bright wave passed the zenith in the OH all-sky images (Figure 1), confirming that both the imager and the MTM were observing me dynamical structure. The OH intensity began to decrease after ~1030 UT and reached a local minimum at 1200 UT. Because the O_2 and OH emissions are centered at ~89 and 94 km, respectively [*Zhao et al.*, 2005], the leading intensity perturbation in the O_2 airglow followed by OH indicates that the perturbation was associated with an upward-propagating gravity wave (downward phase progression). The period of this large-amplitude wave was estimated to be ~4 hours from this data. This 4-hour wave was not identifiable after ~1200 UT. There appeared to be a smaller-scale 1-hour period wave that was superimposed on the large-amplitude wave.

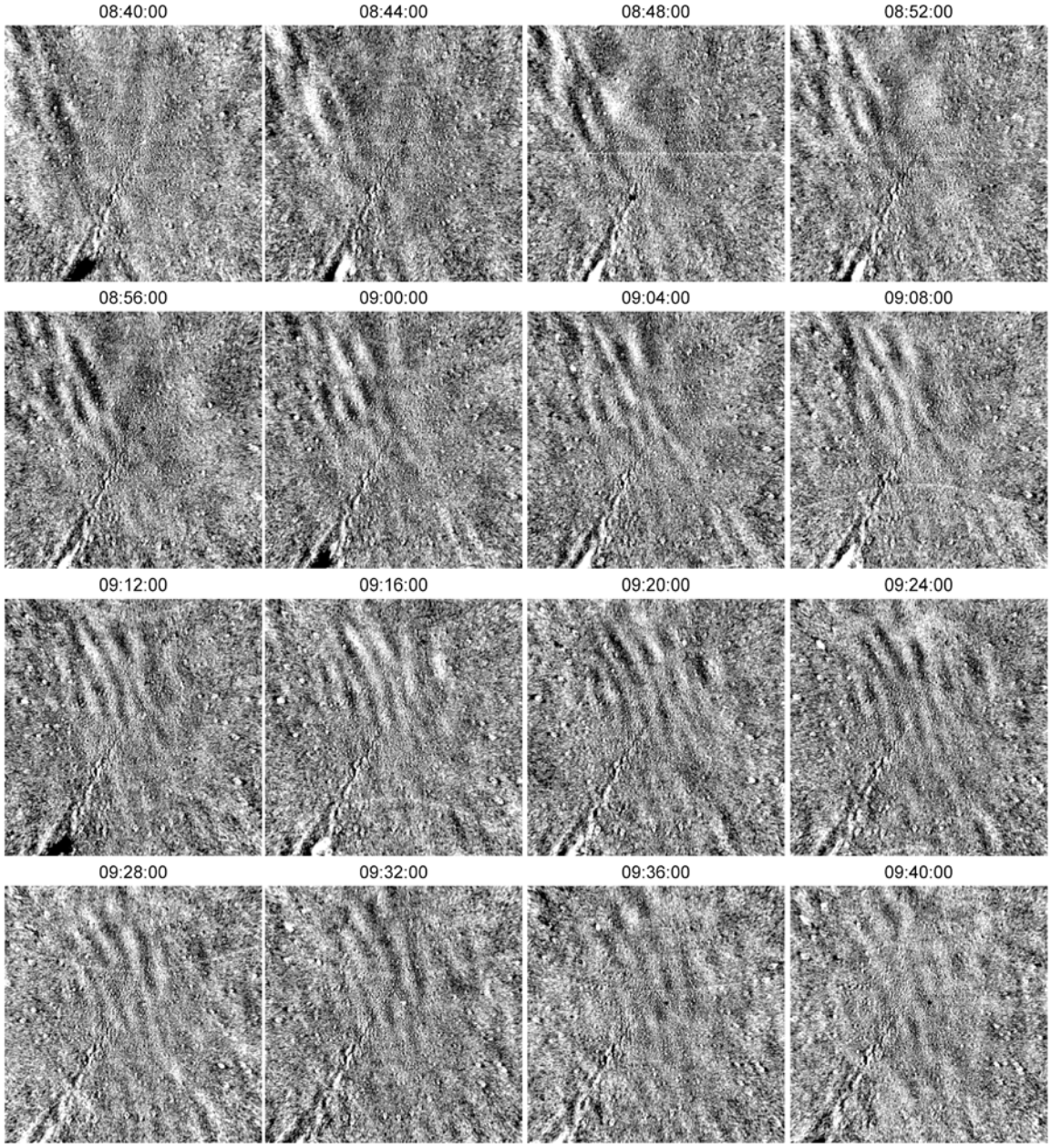

Figure 2. Same as Figure 1, but each image is normalized by dividing the raw image by a background image, which is defined as the average of five consecutive images centered at the image to be normalized.

[15] Also plotted in Figure 3a is the time sequence of the Na abundance measured by the Na lidar system. The Na abundance nearly tripled from ~0800 to 1000 UT, with the sharpest increase centered at ~0900 UT when the bright wave passed the zenith. In contrast to the evolution of airglow intensities, the Na abundance didn't decrease after it reached the maximum.

[16] The changes of airglow intensity and Na abundance associated with the bright wave are very similar to those observed by *Swenson et al.* [1998] (hereinafter referred to as S98). The time history of the airglow brightness looks very much like a "step" function, or a "wall". Hereafter we refer to this bright wave as "wall" wave.

[17] The O_2 and OH rotational temperature also exhibited a very large perturbati ring the passage of the wall wave. Figure 3b shows that both the O_2 and OH rotational temperature increased by ~30 K, but the change in the O_2 rotational temperature led that of the OH rotational temperature by ~1 hour, consistent with the airglow brightness observations and supportive of the upward-propagating wall wave explanation. Before 0900 UT, the O_2 rotational temperature was ~20 K higher than the OH rotational temperature, indicating a strong inversion layer between the OH and O_2 emissions. The difference between the O_2 and OH rotational temperature was significantly reduced after 0900 UT.

[18] We can learn more about the wall wave by comparing with the observations made the night before on 10–11 August 2004 (Figure 4). The two nights showed very different structures in the time evolution of airglow inten-

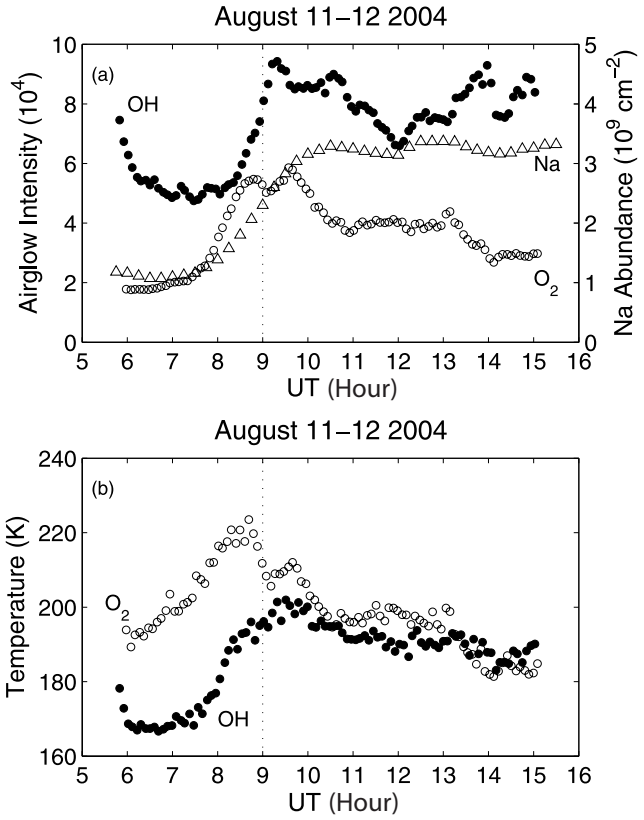

Figure 3. Time series of (a) the MTM zenith OH (solid circles) and O_2 (open circles) intensity and the Na abundance (triangles) and (b) the MTM OH (solid circles) and O_2 (open circles) rotational temperature on the night of 11–12 August 2004. The dotted line at 0900 UT indicates the time when the leading bright front passed the zenith in the all-sky images.

sity, rotational temperature, and Na abundance. The largest discrepancies occurred before ~1000 UT. It was found that, on the wall wave night, the OH and O_2 airglow intensities, and the Na abundance as well, were strongly depleted before ~0800 UT. Before 0800 UT, the mean OH intensity, O_2 intensity, and the Na abundance on the wall wave night were only, respectively, ~50%, 25%, and 40% of those on the night before. The strong depletion of airglow intensities was associated with strong cooling. The OH and the O_2 rotational temperature were ~30 K colder before 0800 UT on the wall wave night than the night before. It appears that the sharp increase associated with the passage of the wall brought the magnitude of airglow intensity, Na abundance, and temperature to a value comparable to the night before.

[19] The observed strong depletion followed by sharp increase of airglow intensity is not explained by the bore theory, which predicts either sharp increase or decrease of airglow brightness, but not both. This observation, however, can be explained by the wall wave theory, where the depletion/cooling and the increase/warming were associated with opposite phases of a large amplitude gravity wave. This will be discussed in detail in section 4.1.

[20] Note that the timescale of the sharp increase for this event is about 1 hour, while the bore events in the literature show timescales of mi or the passage of the leading front. This difference in timescale provides further evidence that this event was not a bore.

3.3. Lidar Observations

[21] As has been mentioned in the introduction, this is the first time a bright wave event was captured by a wind/temperature lidar with high-resolution wind and temperature measurement. The high-resolution wind and temperature measurements make it possible to perform a detailed dynamical analysis of the wall wave.

[22] Figure 5 shows the lidar observations of temperature (T), Na density, and zonal (U) and meridional (V) winds through the night. The most striking feature in temperature is a very large-amplitude wave before 1000 UT centered at ~92 km, with a valley-to-peak amplitude of >60 K (Figure 5a). Figure 5a also suggests that the wall wave had a period of 4–5 hours, which is consistent with the estimated 4-hour period from the MTM observations. The wave amplitude was heavily damped, with the signature of the wave almost unidentifiable after 1200 UT. The wall wave was upward propagating with rapid downward phase progression. The lidar temperature observations were very consistent with the MTM measurements. It is clear that the dramatic changes in the O_2 and OH airglow brightness and rotational temperature (Figure 3) were the projection of the wall wave in the airglow emissions.

[23] The wind structure was more complex, apparently due to the interactions of the 4–5 hour wave with tides. Before 1200 UT, the tidal structure, especially in the zonal wind, was severely disrupted, but it became much more

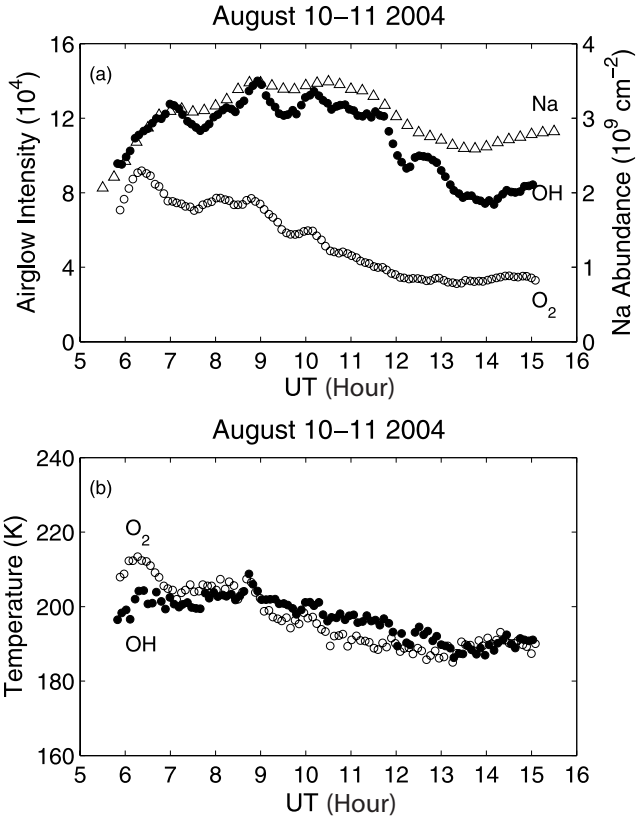

Figure 4. Same as Figure 3, but for the night of 10–11 August 2004.

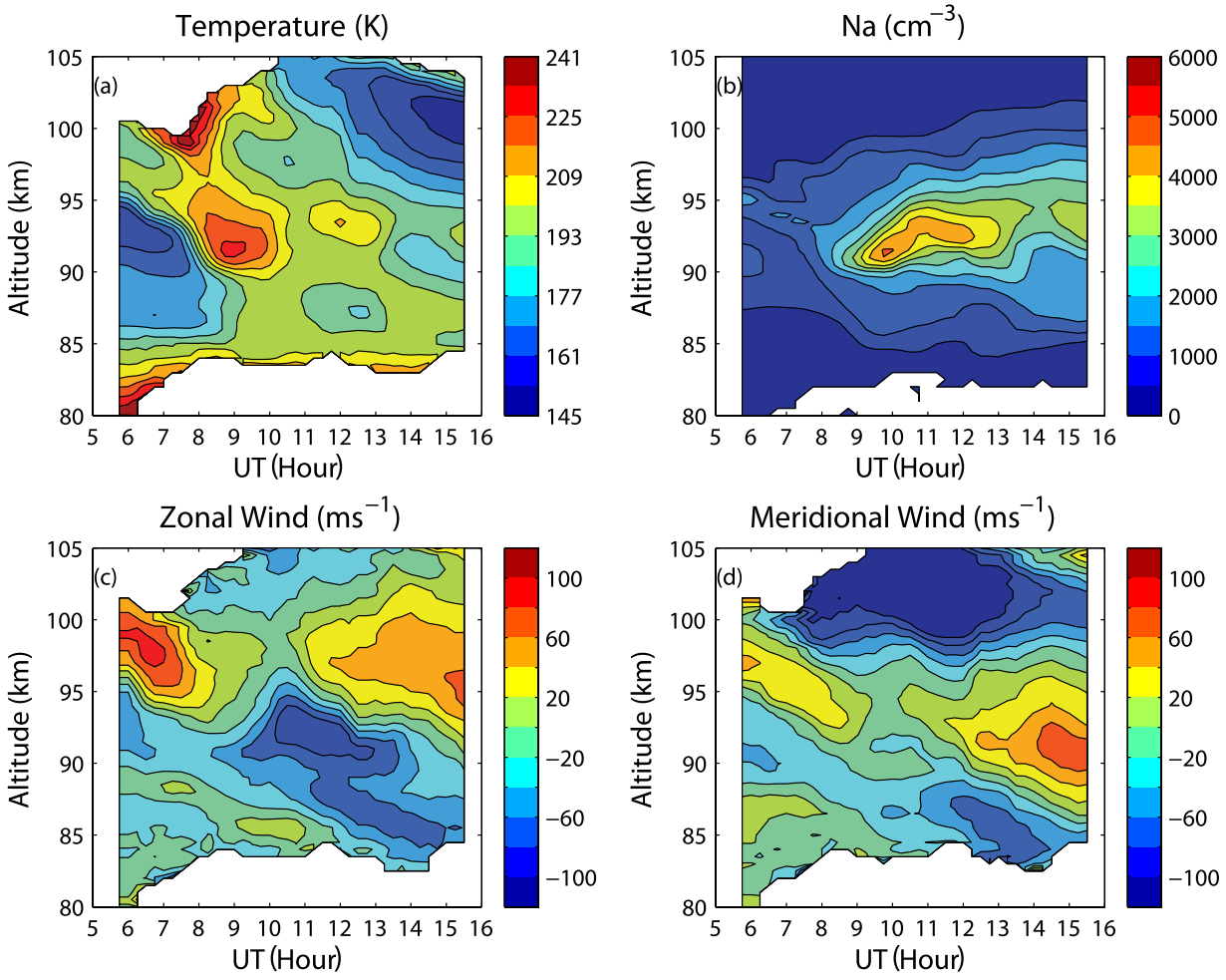

Figure 5. Time-height contours of (a) temperature, (b) Na density, (c) zonal wind, and (d) meridional wind. The data were smoothed using a 1-km and a 1-hour Hamming window vertically and temporally, respectively. The smoothing was done every 0.5 km vertically and every 15 min temporally.

coherent later. The structure of a 4–5 hour period wave can be seen before 1200 UT. Figure 5c shows the signature of the wave in the zonal wind between 90 and 95 km before ~1200 UT, while this wave is more clearly seen between 95 and 100 km in the meridional wind (Figure 5d).

[24] In order to confirm the above result, a power spectrum analysis was performed on the lidar temperature and wind data. The data set is same as that used to plot Figure 5, but the temporal smoothing is performed by binning the data every 15 min. Only data obtained before 1200 UT was used because the wall wave was significantly damped after 1200 UT. The spectrum analysis was done for observations between 85 and 100 km since the measurement uncertainties increase very sharply below 85 and above 100 km. At a given altitude, the linear trend was removed and a periodogram was calculated.

[25] The periodograms of T, U, and V as a function of height are shown in Figure 6. Spectral power maxima in the 4–5 hour range were found in all three variables, which are consistent with above discussions. Very similar vertical variations of the wave amplitude were observed in T, U, and V, with two enhanced spectral power region centered at ~92 km and 99 km. The temperature and zonal wind exhibited a stronger po 92 km than at 99 km, whereas the meridional wind showed a weaker amplitude at 92 km. The periods of maximum power were slightly different among T, U, V. In the temperature, the upper enhanced spectral power was centered at 4 hours, but there appeared to be a frequency shift in the lower region of enhanced power, which was centered between 4 and 5 hours. In the zonal wind, both the 99 and 92 km power spectral density maxima occurred at 5 hour periods, while they were located at 4 hours in the meridional wind. The coincidence of enhanced power spectrum density occurring at 4–5 hour period and at about the same altitude in T, U, and V strongly support the existence of the 4–5 hour period wall wave. The slight difference in the period of maximum power is not surprising. Interactions between the wall wave and other waves, tides for example, can cause changes of the wave period.

[26] The vertical wave structure can be more clearly seen when the background trend is removed. Figure 7 shows the wave structure using two methods for removing the background trend. In Figure 7, top, the mean at each altitude was removed to calculate perturbations. In Figure 7, bottom, time derivatives, which are defined as the difference of two consecutive measurements, are presented. Both methods reveal a coherent downward progression of the 4–5 hour

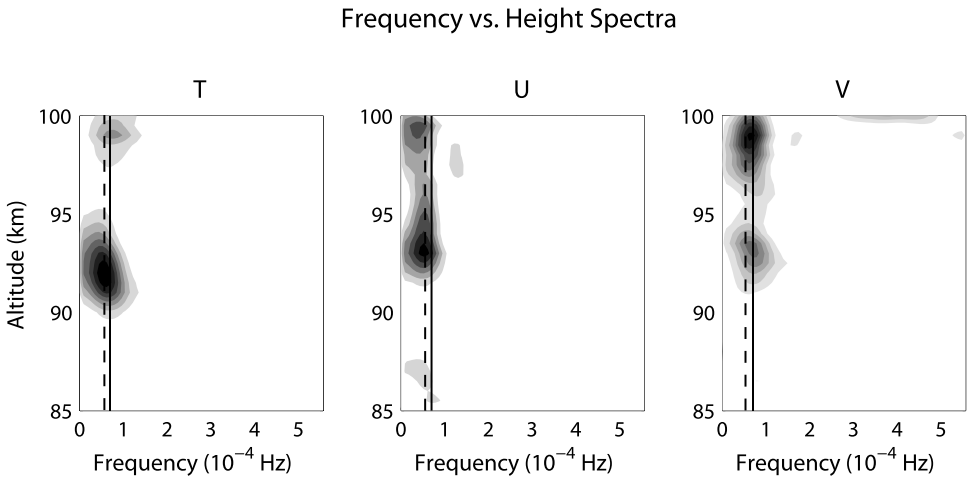

Figure 6. Periodograms of temperature (T), zonal wind (U), and meridional wind (V) as a function of altitude. The dashed and solid lines denote periods of 5 and 4 hours, respectively. The strength of the spectra increases from white (lowest value) to dark (highest value).

wave above 90 km. The average downward phase speed was ~1.2 ms^{-1} (or 4.3 km hr^{-1}), indicating a vertical wavelength between 17 and 22 km. The lidar observations didn't record the structure for the entire vertical wavelength because the wave signature was not clear below 90 km. Figure 7 shows, however, that the half vertical wavelength was ~10 km, in agreement with the downward phase speed. The estimated ~20 km vertical wavelength is also consis-

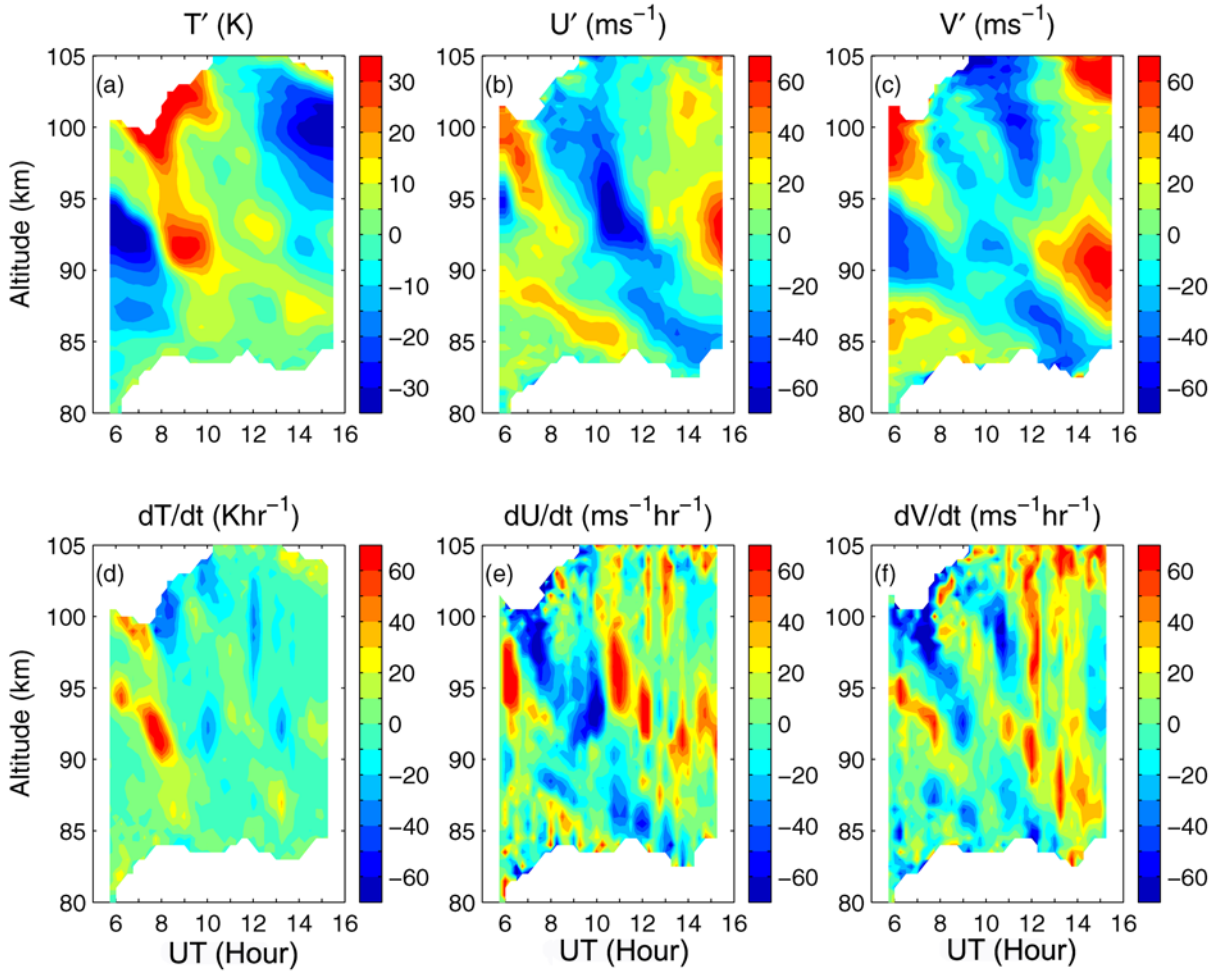

Figure 7. Time-height contours of the (a) temperature perturbation T′, (b) zonal wind perturbation U′, (c) meridional wind perturbation V′, (d) temporal change in temperature dT/dt, (e) temporal change in zonal wind dU d (f) temporal change in meridional wind dV/dt.

Table 1. "Wall" Wave Parameters and the Changes in Airglow Intensity and Rotational Temperature During the Passage of the Wave

Parameters	Value	Instrumentation
Period	4–5 hours	Lidar, MTM
Observed phase speed	45 ms^{-1}	Imager
Intrinsic phase speed at 89 km	85 ms^{-1}	Lidar, Imager
Horizontal wavelength	650–810 km	Lidar, Imager
Vertical wavelength	20 km	Lidar, MTM
Amplitude of relative temperature at 92 km	15%	Lidar
Amplitude of relative OH intensity	31%	MTM
ΔOH intensity	90%	MTM
Amplitude of relative O_2 intensity	47%	MTM
ΔO_2 intensity	175%	MTM
ΔNa abundance	200%	Lidar
ΔT_{O2} rotational temperature	30 K	MTM
ΔT_{OH} rotational temperature	30 K	MTM

tent with the MTM observations. Figure 3 shows that the wall wave in the O_2 emission led the OH emission by ~1 hour. Because the two emissions are separated by ~5 km, the phase difference also suggests a vertical wavelength of ~20 km.

[27] The vertical wavelength can also be deduced from the linear gravity wave dispersion relation

$$m^2 = \frac{N^2}{(C_O - U)^2} - k^2 - \frac{1}{4H^2}, \quad (1)$$

where m is the vertical wave number, N^2 is the buoyancy frequency squared, C_o is the observed phase speed, U is the background wind, k is the horizontal wave number, and H is the density-scale height. The observed phase speed of the leading front of the wall wave was 45 ms^{-1}. A period of 4–5 hours indicates a horizontal wavelength between 650 and 810 km, and the mean value of 730 km was used. The background condition was calculated as the nightly mean. N^2 was computed using the nightly mean temperature profile and H was assumed to be 6 km. In equation (1), the most important factors affecting the wave vertical wavelength is the first term on the right hand side, i.e., N^2 and the intrinsic phase speed $Ci = Co - U$. The calculated vertical wavelength in the 85–100 height range was not constant, but the mean value was 20 km, consistent with the lidar and airglow observations.

[28] Table 1 summarizes the parameters of the wall wave and the changes in airglow brightness and rotational temperature during the passage of the wall. This wave is similar, in many aspects, to the S98 wall wave. Both waves had vertical wavelengths of ~20 km. S98 recorded changes of 85% in OH airglow intensity and 180% in Na abundance, and these numbers are 90% and 200% in the current case. The intrinsic phase speeds in the OH altitude are also close to each other, being 75 ms^{-1} in S98 and 85 ms^{-1} in current case. S98 reported wave magnitude of 10% at 88 km and a wave growth factor of 0.05 km^{-1}, implying the amplitude would be 12% at 92 km, which was smaller, but close to the observed 16% amplitude at 92 km in this case. The most significant differences between the two waves are period and horizontal wavelength. The S98 wall had a shorter period (80 min compared to 4–5 hours) and shorter horizontal wavelength (300– km versus 650–830 km).

[29] In order to test the extracted wall wave parameters, a comparison was performed between the observed and model temperature at two opposite phases. Figure 8 shows observed and modeled temperature profiles in the 85–100 km height range at 0645 and 0900 UT, when the wall wave reached its minimum and maximum temperature, respectively. The modeled temperature was calculated using the following equation [*Liu and Swenson*, 2003],

$$T/T_u = 1 + \varepsilon \exp\left[\frac{1-\beta}{2H}(z - z_0)\right] \cos[m(z - z_0) - \omega t], \quad (2)$$

where T is the modeled temperature, T_u is the unperturbed temperature, ε is the wave amplitude at z_0, β is the damping factor, H is the density-scale height, and $\omega = 2\pi/\tau$ is the wave frequency. The damping factor, β, is introduced to simulate wave dissipation following *Liu and Swenson* [2003]. When $\beta = 0$, the wave amplitude will increase with an e-folding height of $2H$, i.e., without damping. When $\beta = 1$, the wave amplitude will remain constant with height, which is a simplified case for wave saturation. Strong dissipation will occur if $\beta < 1$, as the wave amplitude will decrease with increasing altitude. Parameters used for generating the modeled temperature profiles are based on observations, which include ε = 30 K, z_0 = 92 km, λ_z = 20 km, τ = 4.5 hours. The unperturbed profile T_u is defined

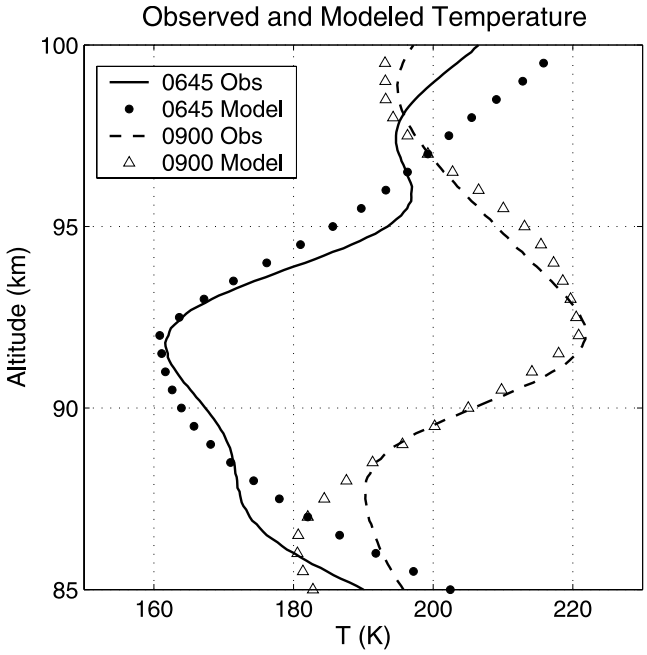

Figure 8. Comparison of the observed (solid and dashed lines) and modeled (circles and triangles) temperature profiles for the opposite phases of the "wall" wave. The solid line/circles is for 0645 UT when the "wall" wave was in the phase of lowest temperature, and the dashed line/triangles is for 0900 UT when the "wall" wave reached highest temperature. The following parameters were used to model the temperature profiles: period of 4.5 hours, vertical wavelength of 20 km, and amplitude of 30 K at 92 km. A damping factor of 1 above 92 km and 0 below 92 km was employed.

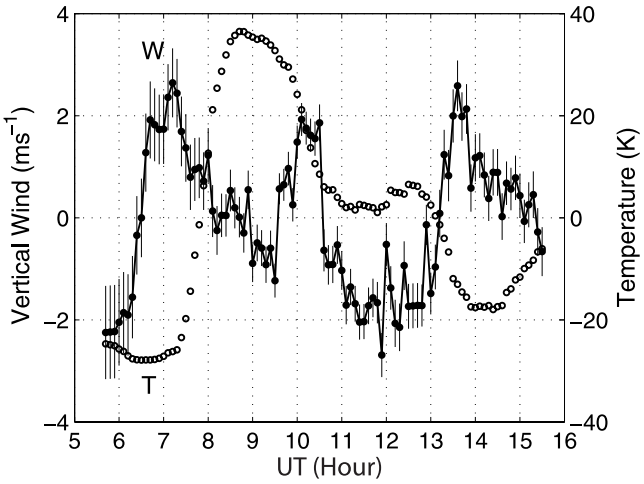

Figure 9. Time series of the vertical wind (solid circles) and temperature (open circles) at 92 km. The linear trend was removed in both series. The thin line indicates the error bar of the vertical wind. Error bars of the temperature are not plotted, but they are smaller than the radius of the circle. The data were temporally smoothed with a 1-hour Hamming window at every 6 min.

as the mean profile before 1000 UT. Figures 4–6 show that the temperature perturbations reached maximum amplitude at 92 km. Therefore it is assumed that the wall wave was not damped below 92 km ($\beta = 0$) but was damped (saturated) above 92 km ($\beta = 1$).

[30] Figure 8 shows that the modeled temperature profiles agree quite well with the observations. The two profiles have opposite phases at 92 km, being separated by 2.25 hours for a wave period of 4.5 hours. The model results almost overlap with the observations in the 87–97 km height range at both phases. For 0900 UT, the agreement extends to 100 km. Although there are discrepancies below 87 km, the general agreement between the observations and the models, especially when considering the simplicity of the model, strongly supports the above analysis of the wall wave.

[31] It is clear that the observed dramatic temperature increase was due to the large gravity wave changing from the minimum temperature phase to the maximum temperature phase. Accordingly, the sharp increase of airglow intensities was directly related to the phase of the wall wave as it propagated through the airglow layers.

4. Discussion

4.1. Sharp Increase of Airglow Intensity

[32] The sharp increase of airglow intensity (90% in OH and 175% in O_2 emission) was determined to be due to the passage of the large amplitude gravity wave. The response of the OH emission to gravity wave perturbations was studied in detail by *Swenson and Gardner* [1998]. A gravity wave can disturb the OH airglow intensity by wave-induced perturbations in species involved in the OH chemistry, primarily the atomic oxygen ([O]), and in temperature that affects the reaction rate. *Swenson and Gardner* [1998] found that the most important mechanism is through wave-induced vertical ort of [O]. This is because [O] has a sharp vertical gradient in the OH airglow altitude. When the wave is in the phase of upward motion, transport of low-[O] air into the OH layer will lead to depletion of airglow intensity. When the phase changes to downward motion, input of rich-[O] air from above will render enhancement of the OH airglow intensity. Downward/upward motion causes adiabatic heating/cooling. As a result, depletion of OH brightness is associated with upward motion and low temperature, while enhancement of OH intensity is related to downward motion and high temperature. Generally, low/high airglow intensity, upward/downward motion, and low/high temperature are not exactly in phase. The actual phase difference among them is a complex function of vertical wavelength and wave dissipation rate [*Liu and Swenson*, 2003]. Although the chemistry of O_2 emission is different from that of the OH emission, [O] is still the most important species through which gravity waves perturb the O_2 airglow intensity [*Liu and Swenson*, 2003]. Hence the above argument also applies to O_2 airglow through the chemical involvement of [O].

[33] Figure 9 shows the time sequences of vertical wind and temperature with linear trend removed at 92 km. The vertical wind exhibited a distinct nearly anticorrelation with the temperature before ~1000 UT. The temperature reached minimum and maximum at ~0645 and 0900 UT, respectively, while the maximum upward and downward motions occurred at ~0700 and 0915 UT, respectively. Figure 3a shows that the OH brightness was lowest at ~0720 UT and highest at ~0920 UT, and similar oscillation was found in the O_2 brightness except for a ~1-hour lead. Since 92 km is in the middle of the nominal value of the peak OH (89 km) and O_2 (94 km) airglow altitude [*Zhao et al.*, 2005], we can take Figure 9 as the mean structure between the OH and O_2 emissions. Therefore the relationships among temperature, vertical wind and airglow intensity are very consistent with the explanation that strong depletion and enhancement of the airglow brightness was caused by gravity wave induced larger perturbations in [O].

4.2. Cancellation Factor: Comparison with a 1-D Model

[34] The response of airglow emission to gravity waves has been extensively studied [e.g., *Krassovsky*, 1972; *Walterscheid et al.*, 1987; *Reisin and Scheer*, 1996]. Historically, these studies focused on the amplitude and phase of the ratio between wave-induced intensity perturbations and rotational temperature perturbations, i.e., the Krassovsky parameter. However, the relationship between airglow intensity perturbations to the gravity wave that induces the perturbation is more relevant to this study.

[35] It is now well known that gravity wave induced airglow intensity perturbations is sensitive to the wave vertical wavelength, especially when the vertical wavelength <10 km. The observed airglow intensity is the line-of-sight integration of wave-perturbed airglow volume emission rate through the whole emission layer. Since both the OH and O_2 emission layers have a full-width-at-half-maximum of ~10 km, for gravity waves with <10 vertical wavelength, integration through the emission layer will result destructive interference. The shorter the wavelength, the stronger the cancellation effect is. *Swenson and Gardner* [1998] developed a theoretical model relating amplitude of

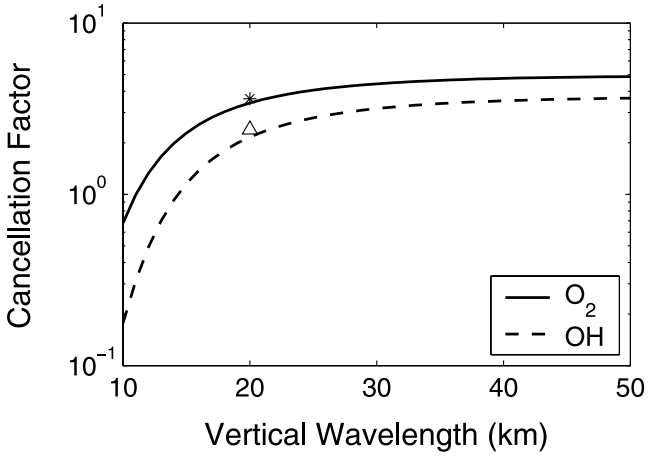

Figure 10. Cancellation factors for O_2 (solid) and OH (dashed) as a function of gravity wave vertical wavelength from the *Liu and Swenson* [2003] model. The wave parameters used in the model include a period of 4.5 hours and a damping factor of 1 ($\beta = 1$ in equation (2)); that is, wave amplitude remains constant with height. The star and triangle denote the cancellation factor of the "wall" wave for the O_2 and OH emissions, respectively.

wave-induced OH airglow perturbations to the wave amplitude, which is called cancellation factor (CF). The cancellation factor is defined as

$$CF = \frac{(I'/\langle I\rangle)_{amplitude}}{(T_w'/\langle T_w\rangle)_{amplitude}}, \quad (3)$$

where the numerator is the amplitude of relative intensity, and the denominator is the wave amplitude in terms of relative temperature. It should be noted for vertical wavelength > about 10 km, the cancellation factor >1; that is, the airglow acts to amplify the airglow signal of gravity waves for long vertical wavelength waves.

[36] The *Swenson and Gardner* [1998] theoretical model only applies for the OH emission. *Liu and Swenson* [2003] developed a 1-d numerical model to study wave perturbations in both the OH and O_2 emissions. Figure 10 plots the cancellation factor for OH and O_2 as a function of vertical wavelength from the *Liu and Swenson* [2003] model. A wave period of 4.5 hours and a damping factor $\beta = 1$ were employed to generate the data. The 4.5 hour period is chosen because the wall wave had a period of 4–5 hours, but in fact the cancellation factor is not sensitive to wave period. The damping factor β has the same meaning as the one in equation (2). Note that in the *Liu and Swenson* [2003] model the damping factor remains constant with height, therefore we cannot change the damping factor as we did in Figure 8. Choosing $\beta = 1$ is under the consideration that the model wave amplitude is about the same (13%) at the peak OH and O_2 airglow layer (being 89.5 and 94.7 km in the Liu and Swenson model) in Figure 8.

[37] The calculated cancellation factors of this wall wave for both the OH and O_2 emissions are in good agreement with the model predictions, providing additional support for the wall wave explanation. Figure 10 shows that for a gravity wave with a m vertical wavelength, the response of airglow emission to wave perturbations is to amplify the wave amplitude by a factor of 2.4 in OH and 3.6 in O_2. Because of this amplifying effect for long vertical wavelengths waves, airglow emissions are excellent for gravity wave studies. The cancellation factor in O_2 is 1.5 times larger than that in OH. This is mainly because the O_2 volume emission rate is proportional to the square of [O], while the OH volume emission rate is proportional to [O]. Since gravity wave induced perturbations in [O] is the dominant mechanism for disturbing airglow emissions, the O_2 is more sensitive to gravity wave perturbations.

4.3. Heat and Momentum Fluxes

[38] Figure 9 shows that the anticorrelation between the vertical wind and the temperature changed after ~1000 UT. Interestingly, the phase relationship between the vertical and the temperature after 1000 UT agreed with the idealized gravity wave dispersion relation with the temperature leading the vertical wind by ~90°.

[39] In the absence of wave dissipation, the perturbations of temperature (T′) and vertical wind (w′) are in quadrature, and hence the wave heat flux $\overline{w'T'} = 0$ [*Walterscheid*, 1981]. Wave dissipation, however, changes the phase relationship between T′ and w′, inducing a net heat flux. *Walterscheid* [1981] showed that net effect of gravity wave dissipation is to induce a downward heat flux ($\overline{w'T'} < 0$), the so-called dynamical cooling. The magnitude of the heat flux is proportional to the wave amplitude and the departure of T′ and w′ from quadrature that is determined by the wave dissipation [*Fritts*, 2000].

[40] Wave heat flux is calculated simply as the covariance between T′ and w′. Calculation of heat flux usually requires long time data average to reduce uncertainties [*Tao and Gardner*, 1995]. *Liu and Gardner* [2005] obtained the mean heat flux profile between 85 and 100 km at Maui using more than 100 hours of lidar temperature and vertical wind measurements. They found there are two maxima at 87 and 95 km, with downward heat flux of 1.25 and 1.40 K ms^{-1}, respectively. The largest heat flux on this night was observed at the same altitude and during the same period when the wall wave was strongest. The mean heat flux profile on this night exhibited two downward maxima at ~92 and 100 km (figure not shown), consistent with the spectral analysis of the wall wave (Figure 6). The amplitude of the heat flux maxima was 10 K ms^{-1} at 92 km and 15 K ms^{-1} at 100 km, much larger than the climatology mean. Another interesting fact is that the mean heat flux between 85 and 100 km before 1000 UT, during which the wall wave in temperature had large amplitude, was −7.4 K ms^{-1}, much stronger than the mean value of −1.4 K ms^{-1} after 1000 UT. These observations clearly demonstrated that dissipation of the wall wave induced huge downward heat flux.

[41] For historical reasons, the effects of gravity wave transport of heat flux are underappreciated. For example, until very recently, none of the major gravity wave parameterization schemes account for differential heating due to gravity wave dissipation. The importance of this effect on the thermal budget in the MLT become more and more clear in recent years by observational, theoretical and numerical studies [e.g., *Gardner and Yang*, 1998; *Liu et al.*, 2000; *Medvedev and Klaassen*, 2003]. *Liu and Gardner* [2005] estimated cooling rate on the order of several tens of degree

per day, which far exceeded exothermic chemical heating [*Hickey and Walterscheid*, 1994]. This wall wave event provides an exceptional case of wave transport of large downward heat flux.

[42] We can also estimate the momentum flux of the wall wave. The momentum flux $\overline{u'w'}$ is calculated using relative temperature perturbations as

$$\overline{u'w'} = \frac{1}{2}\frac{\lambda_z}{\lambda_h}\frac{g^2}{N^2}\left(\frac{T'_w}{\langle T_w\rangle}\right)^2, \quad (4)$$

where λ_z is the vertical wavelength, λ_h is the horizontal wavelength, and $\left(\frac{T'_w}{\langle T_w\rangle}\right)$ is the amplitude of relative temperature [*Swenson and Liu*, 1998]. Given $g = 9.5$ m^2 s^{-2}, $N = 0.02$ s^{-1}, $\lambda_h = 730$ km, $\lambda_z = 20$ km, and $\left(\frac{T'_w}{\langle T_w\rangle}\right) = 0.15$ (from Table 1), the momentum flux of the wall wave is estimated to be $\sim$70 m^2 s^{-2}. This value is much larger than the mean momentum flux of $\sim$20 m^2 s^{-2} associated with high-frequency (period <30 min) gravity waves [*Swenson et al.*, 1999]. However, it should be noted that, in general, low-frequency waves are much less efficient than high-frequency waves in upward transporting momentum flux because of their shallow propagation path.

4.4. Comparison with the Mesospheric Bore Theory

[43] Some features of this bright event, e.g., the presence of a temperature inversion layer, significant changes in airglow intensity, trailing waves phase locked with the leading front, and the increase of trailing wave crests with time, seem also be consistent with the mesospheric bore explanation. The analyses in section 3 and section 4.1, however, have clearly demonstrated that this event was due to a large-amplitude long-period upward-propagating gravity wave, and it is not characteristic of a bore event.

[44] The existence of a temperature inversion layer is crucial for the bore theory because it provides a duct for the bore, although it should be emphasized that an inversion layer is a necessary, but not a sufficient condition for a bore. On the other hand, the existence of a temperature inversion layer is not required in the wave theory, but it's not surprising if an inversion layer is present during the passage of the wall wave. In this event, a strong temperature inversion layer existed in the OH and O_2 emission layers before $\sim$1000 UT (Figures 3b, 5a, and 8). This inversion layer was caused by the wall wave, and it progressed downward with the wall wave (Figures 5a and 8).

[45] The characteristics of the change in airglow brightness and temperature in this event, including the timescale, the phase relation of the changes between the OH and O_2 emissions, and the airglow intensity depletion and cooling prior to the passage of the front, do not agree with the bore theory.

[46] The timescale of the sharp increase of the airglow intensity is different between this event and the bore events. All of the bore events in literature show timescale of minutes for the passage of the leading front, whereas this gravity wave event took about 1 hour to increase (Figures 1 and 3).

[47] In the bore theory, the large changes in airglow intensity and temperature are caused by a hydraulic jump that pushes airglow emissions downward or upward depending on the relative locations of the bore channel and the emission. As a result, the changes in airglow emissions at different altitudes are either in phase or 180° out of phase [*Dewan and Picard*, 1998]. Figure 3 shows that the changes of airglow intensity and temperature in the OH and O_2 airglow was not in phase, nor antiphase, but was $\sim$90° out of phase with the changes in the O_2 emission leading that in the OH emission by $\sim$1 hour. This phase difference between the two layers is consistent with an upward-propagating gravity wave having a vertical wavelength of 20 km and a period of 4–5 hours, because the two layers are separated by $\sim$5 km. Figure 7 provides the most direct and convincing support for the wall wave explanation, showing consistent downward progression in temperature and the horizontal winds.

[48] The bore theory also cannot explain the observed strong airglow intensity depletion and temperature decrease prior to the passage of the wall (Figure 3). The bore induces either decrease or increase in airglow intensity and temperature, but not both. This feature, however, can be simply accounted for by the wall wave. Figure 8 shows that the cooling is because the wall wave was in the phase of minimum temperature.

[49] Most features of this event have been explained by the wall wave theory, but the mechanism for one interesting structure, the apparent phase locking of the trailing high-frequency wave bands with the bright front, remains unclear to us. Most likely this phenomenon was not a coincidence. There are several possible explanations. One hypothesis is that the high-frequency waves were secondary waves induced by the breaking or dissipation of the wall wave [*Fritts et al.*, 2002]. Another possibility is that a bore process might be involved, possibly caused by the wall wave. It is also possible that the two waves were generated by the same source such that they had the same phase velocity. Clearly, new theoretical and modeling studies are needed to explore this phenomenon.

[50] Figure 2 shows that the number of trailing wave bands increased with time. It appears to us that the increase of the trailing waves was because more waves became visible beyond the horizontal and propagated into the imager field of view. However, if a bore was involved in the generation of the trailing waves, then formation of new waves due to dissipation of bore energy could also contribute to the overall increase of trailing waves [*Smith et al.*, 2003].

5. Summary

[51] Simultaneous measurements of the mesopause region from an all-sky imager, a mesosphere temperature mapper, and a wind/temperature lidar were obtained during the passage of a bright wave event in airglow. Although there have been a few reports of the mesospheric frontal structures in airglow observations, this was the first time such an event was captured by a wind/temperature lidar. The observations strongly indicate that this event was a large-amplitude propagating gravity wave with a period of 4–5 hours and a vertical wavelength of 20 km, i.e., a wall wave which was first observed by *Swenson et al.* [1998].

[52] Dramatic increase in airglow intensity, Na density, and temperature were recorded when the wall wave passed the zenith of the sky. It is demonstrated that the observed

~60 K increase of temperature was due to the wall wave changing from the minimum temperature phase to the maximum temperature phase. The sharp increase in airglow intensity was also related to the reversal of the wave phase. When the wall wave was in the phase of upward motion, input of low-[O] air into the airglow emission layers from below resulted in strong depletion of airglow intensity. When the wave phase changed to downward motion, the downward transport of rich-[O] led to increase of airglow intensity. This explanation was supported by two observations: 1, the time evolution of vertical wind was almost 180° out-of-phase with that of airglow intensity, and 2, the observed ratio between airglow intensity perturbation amplitude and the wave amplitude, the so-called cancellation factor, is consistent with theoretical and modeling predictions.

[53] In our opinion, future bright wave studies should emphasize more on their effects upon tides and mean flow. Given their large amplitude, bright waves can play an important role in modifying the local thermal and dynamical state through wave tidal/mean flow interactions. In this event, the large heat flux associated with the wall wave (>5 times the climatology mean) could induce a large cooling rate and/or generate a mesospheric inversion layer. The wind amplitude of the wall wave was comparable to or even larger than the tidal amplitude, and hence can significantly disturb the local tidal structure. With the development of new technologies and instruments, complete horizontal and vertical wave structure information and high-quality multiple day and night observations of wind and temperature will become available, and a more thorough understanding of these issues will be achieved in the future.

[54] **Acknowledgments.** This University of Illinois group has been supported by the NSF Atmospheric Sciences grant NSF ATM 0338425 and NASA grants NAG 5-12952 and NAG 5-13593. Operational support for the USU was provided by NSF CEDAR ATM-0003218. Y. Zhao was partially supported as a postdoctoral fellow under NSF grant ATM-0228914.

References

Brown, L. B., A. J. Gerrard, J. W. Meriwether, and J. J. Makala (2004), All-sky imaging observations of mesospheric fronts in OI 557.7 nm and broadband OH airglow emissions: Analysis of frontal structures, atmospheric background conditions, and potential sourcing mechanisms, *J. Geophys. Res.*, *109*, D19104, doi:10.1029/2003JD004223.

Chu, X., C. S. Gardner, and S. J. Franke (2005), Nocturnal thermal structure of the mesosphere and lower thermosphere region at Maui, Hawaii (20.7°N), and Starfire Optical Range, New Mexico (35°N), *J. Geophys. Res.*, *110*, D09S03, doi:10.1029/2004JD004891.

Dewan, E. M., and R. H. Picard (1998), Mesospheric bores, *J. Geophys. Res.*, *103*, 6295–6306.

Fritts, D. C. (2000), Errant inferences of gravity wave momentum and heat fluxes using airglow and lidar instrumentation: Corrections and cautions, *J. Geophys. Res.*, *105*, 22,355–22,360.

Fritts, D. C., S. L. Vadas, and Y. Yamada (2002), An estimate of strong local body forcing and gravity wave radiation based on OH airglow and meteor radar observations, *Geophys. Res. Lett.*, *29*(10), 1429, doi:10.1029/2001GL013753.

Gardner, C. S., and W. Yang (1998), Measurements of the dynamical cooling rate associated with the vertical transport of heat by dissipating gravity waves in the mesopause region at the Starfire Optical Range, New Mexico, *J. Geophys. Res.*, *103*, 16,909–16,926.

Hecht, J. H. (2004), Instability layers and airglow imaging, *Rev. Geophys.*, *42*, RG1001, doi:10.1029/2003RG000131.

Hickey, M. P., and R. L. Walterscheid (1994), Wave modified exothermic heating in the mesopause region, *Geophys. Res. Lett.*, *21*, 2413–2416.

Krassovsky, V. I. (1972), Infrasonic variations of the OH emission in the upper atmosphere, *Ann. Geophys.*, *28*, 739–746.

Li, F., A. Z. Liu, G. R. Swenson, J. H. Hecht, and W. A. Robinson (2005), Observations of gravity wave breakdown into ripples associated with dynamical instabilities, *J. Geophys. Res.*, *110*, D09S11, doi:10.1029/2004JD004849.

Liu, A. Z., and C. S. Gardner (2005), Vertical heat and constituent transport in the mesopause region by dissipating gravity waves at Maui, Hawaii (20.7°N), and Starfire Optical Range, New Mexico (35°N), *J. Geophys. Res.*, *110*, D09S13, doi:10.1029/2004JD004965.

Liu, A. Z., and G. R. Swenson (2003), A modeling study of O_2 and OH airglow perturbations induced by atmospheric gravity waves, *J. Geophys. Res.*, *108*(D4), 4151, doi:10.1029/2002JD002474.

Liu, H.-L., M. E. Hagan, and R. G. Roble (2000), Local mean state change due to gravity wave breaking modulated by the diurnal tide, *J. Geophys. Res.*, *105*, 12,381–12,396.

Medeiros, A. F., M. J. Taylor, H. Takahashi, P. P. Batista, and D. Gobbi (2001), An unusual airglow wave event observed at Cachoeira Paulista 23°S, *Adv. Space Res.*, *27*(10), 1749–1754.

Medvedev, A. S., and G. P. Klaassen (2003), Thermal effects of saturating gravity waves in the atmosphere, *J. Geophys. Res.*, *108*(D2), 4040, doi:10.1029/2002JD002504.

Meriwether, J. W. (1984), Ground based measurements of mesospheric temperatures by optical means, in *MAP Handbook*, vol. 13, pp. 1–18, SCOSTEP Secr., Univ. of Ill., Urbana-Champaign.

Reisin, E. R., and J. Scheer (1996), Characteristics of atmospheric waves in the tidal period range derived from zenith observations of the O2 (0,1) Atmospheric and OH (6-2) airglow at lower midlatitudes, *J. Geophys. Res.*, *101*, 21,223–21,232.

Rezaul, H., and G. R. Swenson (1999), Extraction of motion parameters of gravity-wave structures from all-sky OH image sequences, *Appl. Opt.*, *38*, 4433–4442.

Smith, S. M., M. J. Taylor, G. R. Swenson, C. She, W. Hocking, J. Baumgardner, and M. Mendillo (2003), A multidiagnostic investigation of the mesospheric bore phenomenon, *J. Geophys. Res.*, *108*(A2), 1083, doi:10.1029/2002JA009500.

Smith, S. M., J. S. Friedman, S. Raizada, C. A. Tepley, J. Baumgardner, and M. Mendillo (2005), Evidence of mesospheric bore formation from a breaking gravity wave event: Simultaneous imaging and lidar measurements, *J. Atmos. Sol. Terr. Phys.*, *67*, 345–356.

Swenson, G. R., and P. J. Espy (1995), Observations of two-dimensional airglow structure and Na density from the ALOHA, October 9, 1993, "storm flight", *Geophys. Res. Lett.*, *22*, 2845–2848.

Swenson, G. R., and C. S. Gardner (1998), Analytical models for the response of mesospheric Na and OH layers to atmospheric gravity waves, *J. Geophys. Res.*, *103*, 6271–6294.

Swenson, G. R., and A. Z. Liu (1998), A model for calculating acoustic gravity wave energy and momentum flux in the mesosphere from OH airglow, *Geophys. Res. Lett.*, *27*, 875–878.

Swenson, G. R., and S. B. Mende (1994), OH emission and gravity waves (including a breaking wave) in all-sky imagery from Bear Lake, UT, *Geophys. Res. Lett.*, *21*, 2239–2242.

Swenson, G. R., J. Qian, J. M. C. Plane, P. J. Espy, M. J. Taylor, D. N. Turnbull, and R. P. Lowe (1998), Dynamical and chemical aspects of the mesospheric Na "wall" event on October 9, 1993 during the ALOHA campaign, *J. Geophys. Res.*, *103*, 6361–6380.

Swenson, G. R., R. Haque, W. Yang, and C. S. Gardner (1999), Momentum and energy fluxes of monochromatic gravity waves observed by an OH imager at Starfire Optical Range, New Mexico, *J. Geophys. Res.*, *104*, 6067–6080.

Tao, X., and C. S. Gardner (1995), Heat flux observations in the mesopause region above Haleakala, *Geophys. Res. Lett.*, *22*, 2829–2832.

Taylor, M. J., and M. A. Hapgood (1990), On the origin of ripple-type wave structure in the OH nightglow emission, *Planet. Space Sci.*, *38*, 1421–1430.

Taylor, M. J., D. N. Turnbull, and R. P. Lowe (1995), Spectrometric and imaging measurements of a spectacular gravity wave event observed during the ALOHA-93 campaign, *Geophys. Res. Lett.*, *20*, 2849–2852.

Taylor, M. J., W. R. Pendleton Jr., S. Clark, H. Takahashi, D. Gobbi, and R. A. Goldberg (1997), Image measurements of short-period gravity waves at equatorial latitudes, *J. Geophys. Res.*, *102*, 26,283–26,299.

Walterscheid, R. L. (1981), Dynamical cooling induced by dissipating internal gravity waves, *Geophys. Res. Lett.*, *8*, 1235–1238.

Walterscheid, R. L., G. Schubert, and J. M. Straus (1987), A dynamical-chemical model of wave-driven fluctuations in the OH nightglow, *J. Geophys. Res.*, *92*, 1241–1254.

Walterscheid, R. L., J. H. Hecht, R. A. Vincent, I. M. Reid, J. Woithe, and M. P. Hickey (1999), Analysis and interpretation of airglow and radar observations of quasi-monochromatic gravity wave in the upper mesosphere and lower thermosphere over Adelaide (35°S, 138°E), *J. Atmos. Sol. Terr. Phys.*, *61*, 461–478.

Zhao, Y., M. J. Taylor, and X. Chu (2005), Comparison of simultaneous Na lidar and mesospheric nightglow temperature measurements and the effects of tides on the emission layer heights, *J. Geophys. Res.*, *110*, D09S07, doi:10.1029/2004JD005115.

F. Li, Geophysical Fluid Dynamics Laboratory, Princeton Forrestal Campus, 201 Forrestal Road, Princeton, NJ 08540, USA. (fengl@princeton.edu)

A. Z. Liu and G. R. Swenson, Department of Electrical and Computer Engineering, University of Illinois at Urbana-Champaign, 1308 West Main, Urbana, IL 61801, USA.

M. Taylor and Y. Zhao, Center for Atmospheric and Space Sciences, Utah State University, Logan, UT 84322, USA.